PAPER

Check for updates

Integration of capillary vibrating sharp-edge spray ionization as a nebulization device for ICP-MS†

Tristen L. Taylor and Alexander Gundlach-Graham ID *

This work presents the first use of capillary vibrating sharp-edge spray ionization (cVSSI) as a nebulization technique for inductively coupled plasma mass spectrometry (ICP-MS). When used for ICP-MS sample introduction, cVSSI acts as a low-flow, in-line, continuous nebulization source. cVSSI differs from conventional pneumatic nebulizers in that the nebulization process is independent from the carrier gas used to transport nebulized aerosols into the plasma. To integrate cVSSI with ICP-MS, we constructed a sample introduction chamber using fused deposition modeling; the design, manufacturing, and operation of this chamber will be discussed. We demonstrate the utility of cVSSI as a nebulization device for ICP-MS analysis through characterization of device performance in terms of produced droplet size distribution, sample introduction efficiency, analytical sensitivity, detection limits, linear working range, and long-term stability. With our cVSSI sample introduction system, sensitivity for Ce was 1.98×10^4 counts s^{-1} ng^{-1} mL^{-1} at a sample flow rate of 15 µL min^{-1} with an absolute sensitivity of 5.24×10^{17} counts g^{-1}. Signal stability is observed to have a relative standard deviation of less than 10% across a 45 minutes measurement.

Introduction

For a liquid sample to be measured by inductively coupled plasma mass spectrometry (ICP-MS), it must be transformed into an aerosol by nebulization and then transported into the plasma. An ideal sample introduction system for ICP-MS creates an aerosol of droplets of uniform size with a median diameter from ~5–10 µm, and subsequently transports these droplets with high efficiency to the ICP without compromising plasma stability.[1,2] Due to the simplicity of operation and moderate cost, pneumatic nebulization is the most popular method of liquid sample introduction for ICP-MS. Pneumatic nebulizers create an aerosol by the interaction of a high-velocity gas with a stream of liquid sample. Many types of pneumatic nebulizers have been developed, including concentric, cross flow, and parallel path nebulizers.[3,4] Improvements in nebulizer designs and reduction of the inner capillary size has led to the development of micro-flow nebulizers.[5–7] These systems have made it common practice to introduce liquid samples at rates on the order of tens of microliters per min, which allows for the analysis of small volume samples. Nebulization at low flow rates is also necessary for the coupling of ICP-MS to separation methods such as capillary electrophoresis (CE) and high-performance liquid chromatography (HPLC) to match the liquid flow rates and preserve the resolution of the separation approaches.[8] For example, micro-

bore HPLC separations are performed at flow rates typically below 100 µL min^{-1}.[8] On the other hand, the electroosmotic flow in CE is much lower, from 1–100 nL min^{-1}, and so a make-up solution with a flow rate on the order of microliters per minute is typically used for the combination of CE with ICP-MS.[9]

Although widely used, pneumatic nebulization is not without limitations. One of the main limitations of pneumatic nebulization is low transport efficiency due to the removal of droplets in the spray chamber. Spray chambers discriminate droplets by momentum, removing droplets that are too large, too fast, or too slow.[10] This leads to only a small portion of the nebulized sample entering the plasma and being detected. For nebulizers that operate at higher flow rates (>500 µL min^{-1}), transport efficiency can be as low as 1%.[1] Higher efficiency systems that operate at lower flow rates usually produce smaller droplets, which improves transport efficiency significantly. High efficiency nebulizers have been reported to have 93% of aerosol volume contained in droplets under 10 µm in diameter, compared to 21% for a cross flow nebulizer at the same sample flow rate.[11] Using a high efficiency nebulizer and a Scott-type double pass spray chamber operated at a flow rate of 11 µL min^{-1}, transport efficiencies of nearly 60% have been reported.[12]

Specific nebulizers have been designed to combat that issue of low transport efficiency. These include direct injection nebulizers (DIN),[13–15] which introduce sample directly into the plasma, and torch integrated sample introduction systems (TSIS),[16–18] which use a small volume spray chamber to minimize sample loss. Although both the DIN and TSIS are capable of operating at total consumption, these systems can suffer from incomplete

Department of Chemistry, Iowa State University, USA. E-mail: alexgg@iastate.edu

† Electronic supplementary information (ESI) available. See DOI: https://doi.org/10.1039/d2ja00384h

This journal is © The Royal Society of Chemistry 2023

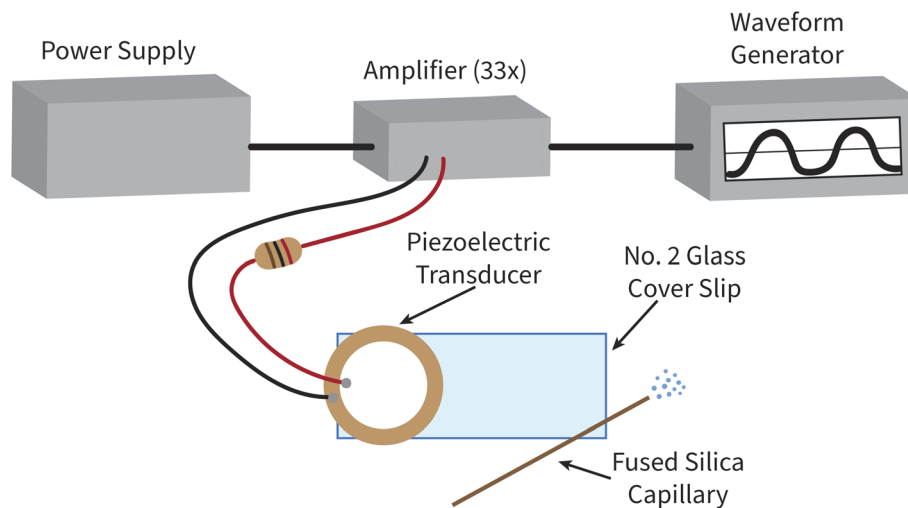*J. Anal. At. Spectrom.*, 2023, 38, 721–729 | 721

Fig. 1 Schematic of sample introduction system showing the cVSSI device and simplified circuit diagram.

vaporization and ionization of droplets in the plasma, which can lead to unstable plasma conditions.[19,20] Transport efficiency into the plasma can also be improved by the use of a desolvation system. These systems can both ensure that smaller droplets are being introduced to the plasma and minimize solvent loading, which promotes stable plasma conditions.[19]

Liquid sample introduction systems that generate an aerosol by means other than pneumatic action are also well established for ICP-MS, but are less wildly used. Ultrasonic nebulizers,[21] monodisperse droplet generators,[22] and thermal inkjet-based nebulizers[23] are examples of these non-pneumatic nebulizers. In these approaches, the nebulization event is separate from the gas flows, which allows for more flexibility in designing sample transport systems and controlling desolvation mechanisms. For monodisperse droplet generators, in particular, the use of helium or heat in a desolvation tube has shown to completely dry droplets and achieve 100% transport efficiency into the plasma.[24-26] In this work, we introduce the use of a new non-pneumatic nebulizer and demonstrate its application for ICP-MS analysis.

Developed by Ranganathan et al., capillary vibrating sharp-edge spray ionization (cVSSI) is a nebulization and ionization device that has been used as a soft ionization source for molecular mass spectrometry.[27] cVSSI devices consist of a microscope glass coverslip, a piezoelectric transducer, and a fused silica capillary, along with driving electronics to power the piezoelectric transducer. The capillary and piezoelectric transducer are attached to the coverslip using epoxy with the capillary attached across the corner of the slide opposite to the transducer. Device to device cost for the cVSSI is very low (~$3/device), and a schematic of the cVSSI device used in our work is presented in Fig. 1. When the piezoelectric transducer is powered at an optimal working frequency, an aerosol is created by the mechanical vibrations at the outlet of the capillary. Since the development of cVSSI in 2019, several applications for mass spectrometry have been explored, including uses in droplet

hydrogen/deuterium exchange, liquid chromatography, solid phase microextraction, and native biomolecule analysis.[28-32]

Here, we present the first application of cVSSI as a nebulization device for ICP-MS, and also discuss the fused deposition modeling (3D printing) of a sample introduction chamber to interface the cVSSI nebulization device with the ICP. Previous studies have shown the feasibility of using fused deposition modeling to create spray chambers for ICP-MS. Thompson demonstrated the ability to 3D model, print, and use cyclonic spray chambers for ICP optical emissions spectroscopy.[33] Geertsen et al. 3D printed cyclonic spray chambers with varying baffle and nebulizer arm measurements to demonstrate the ability of 3D printing for quick prototyping and testing of spray chamber designs.[34]

Experimental

Device fabrication and operation

cVSSI nebulization devices are fabricated as previously described,[27] with adjustments made to the thickness of the glass coverslip to increase the durability of the device. Briefly, a piezoelectric transducer (Murata Electronics, Smyrna, GA, USA) is attached to a no. 2 microscope glass coverslip (Globe Scientific Inc., Mahwah, NJ, USA) using a two-part epoxy (Dev-con, Danvers, MA, USA). Approximately 6 cm of fused silica capillary (Agilent, Santa Clara, CA, USA) measuring 360 μm O.D. and 100 μm I.D. is attached across the distal corner of the coverslip using cyanoacrylate (RapidFuse, Baltimore, MD, USA). The outlet of the capillary is cut at an angle to provide a greater surface area for nebulization. To facilitate this, the capillary is placed on the benchtop and pressure is applied with a ceramic scribe column cutter (Agilent Technologies, Santa Clara, CA, USA) held at an angle to break the capillary outlet. After optimizing capillary parameters such as length, attachment angle, and overhang, 3D printed device molds were created and used for fabrication to ensure reproducibility. A schematic of the cVSSI nebulization system can be seen in Fig. 1 and a picture of

the device with optimized parameters is supplied as Fig. S1 in the ESI.†

Circuitry to power the device has been previously described.[27,35] For our device, sinusoidal waveforms with no DC offset are generated by a Hewlett Packard 33120A Arbitrary Waveform Generator (Agilent, Santa Clara, CA, USA). Sinusoidal waves are used for this work, but square waves and modulated square waves were also tested. AC waves have user set peak voltage and are amplified $33\times$ using a high-power monolithic OPA541 amplifier (Burr-Brown, Tucson, AZ, USA) with support electronics and heat sink on a printed circuit audio amplifier board (Taidacent, Shenzhen Taida Century Technology, Guangdong, China). The amplifier is powered with ± 25 V by a Teledyne T3PS33203 DC power supply (Teledyne LeCroy, Chestnut Ridge, NY, USA). To limit the current through the piezoelectric transducer and overheating of the device, a 110 Ω resistor is placed in series between the OPA541 output and the piezoelectric transducer. Fig. 1 shows a simplified schematic of the circuitry. cVSSI driving waveform characteristics vary from device to device but are usually within 93–98 kHz and 13–27 V_{p-p} after amplification. The working frequency range for each device is found *via* bench top test by visual observation of nebulization using a syringe pump (Harvard Apparatus, Holliston, MA, USA) for sample delivery. The range that a device can nebulize in is typically within ± 1 kHz of the optimum frequency at 20 V_{p-p}.

Chamber design and fabrication

To integrate cVSSI as a nebulization device for ICP-MS, a custom sample introduction chamber was created. The chamber was designed in computer-aided design (CAD) software (Autodesk Fusion360, San Diego, CA, USA) and then manufactured with fused deposition modeling using a dual extruder 3D printer (Ultimaker S3, Utrecht, Netherlands). Polylactic acid (Ultimaker, Utrecht, Netherlands) was used as the build material and polyvinyl acid (Ultimaker, Utrecht, Netherlands) was used as the material for structural supports. After printing, the supports were dissolved in warm water, and additional features such as threaded inserts and O-rings were fitted to the chamber. Gas tubes and wires were attached to the chamber using two-part epoxy (Devcon, Danvers, MA, USA). Additionally, a bracket was designed to hold the nebulization device and fluid connections in place during operation and printed using the same materials.

A schematic of the 3D-printed chamber is shown in Fig. 2. The chamber introduces nebulized aerosol on axis to the ICP and has two compartments: the device-housing chamber and the aerosol-transport chamber, which are connected by a small rectangular opening through which the end of the coverslip and the capillary of the cVSSI device are positioned. The device-housing chamber contains the nebulization device and all fluidic and electrical connections. Argon is introduced as a carrier gas into the back of the device-housing chamber through two 6 mm diameter gas ports. This gas flushes the chamber, assists with sample transport, and prevents the backflow of sample aerosol to the electronic components such

as the piezoelectric transducer. The aerosol-transport chamber houses the capillary outlet at which nebulization occurs. Argon is introduced directly into the aerosol-transport chamber through a ring of equally spaced gas inlets around the rectangular opening between the two chambers; this argon gas flow is termed the curtain gas. Fig. 2B shows the path of the curtain gas into the chamber. The aerosol-transport chamber outlet is designed to fit into the torch/injector mount of the ICP-MS instrument with an O-ring to ensure a gastight seal. The entire introduction chamber is supported by a custom bracket mounted to the ICP-MS instrument using the threaded inserts intended for support of a Peltier cooler block. Fig. S2† shows an image of the sample introduction system on the ICP-MS instrument.
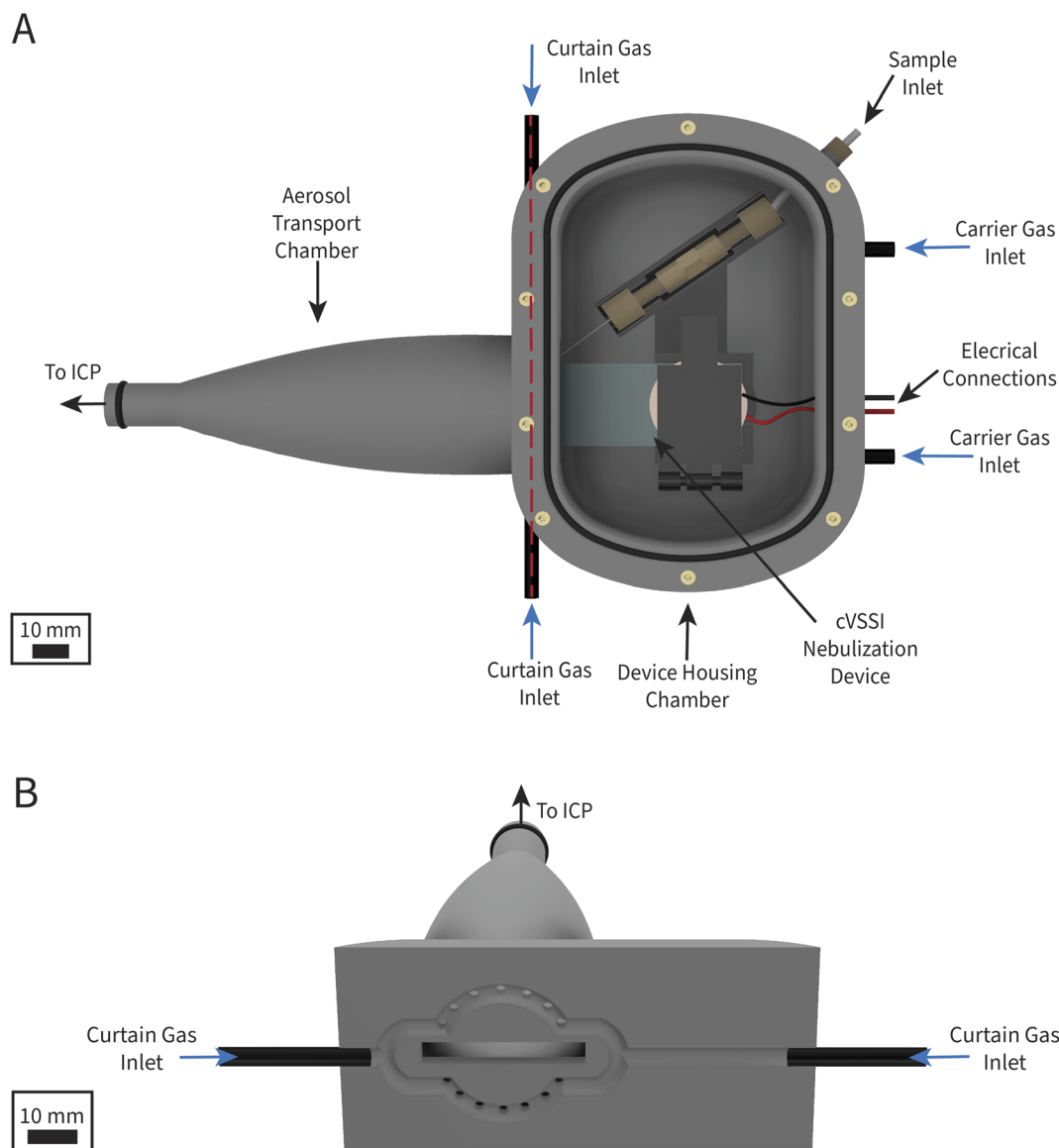
Instrumentation

Measurements for this work were collected with an inductively coupled plasma time-of-flight mass spectrometry (ICP-TOFMS) instrument (icpTOF-S2, TOFWERK AG, Thun, Switzerland). Samples were introduced with a microFAST MC autosampler (Elemental Scientific Inc., Omaha, NE, USA). Argon was introduced into the 3D-printed chamber using both the nebulizer gas port on the icpTOF instrument and an external mass flow controller (FMA-A206-SS, Omega Engineering Inc., Norwalk, CT, USA). The sample introduction chamber was flushed for at least thirty minutes with 300 mL min^{-1} of Ar before igniting the plasma, and argon flow through the external gas supply was kept on during the plasma ignition. Operating parameters for each experiment are provided in Table S1.†

Reagents and sample preparation

Dissolved element samples were prepared from single-element standards (High-Purity Standards, North Charleston, SC, USA). Elements used were Co, Y, In, Cs, Ce, Er, Bi, and U. Ultra-uniform gold nanoparticles (AuNPs, 50 nm diameter) for transport studies were purchased from nanoComposix (now Fortis Life Sciences, San Diego, CA, USA). Solutions containing only dissolved elements were diluted in 1% trace metal grade nitric acid (Fisher Scientific, USA) that is purified in house by sub-boiling distillation (DST-1000, Savillex Corp., MN, USA). Samples containing both nanoparticles and dissolved elements were diluted in ultrapure water (18.2 MΩ cm PURELAB flex, Elga LabWater, High Wycombe, UK). All sample solutions were prepared gravimetrically on the day measurements were taken.

Multi-element calibration solutions were prepared from 0.5 to 100 ng mL^{-1}, and a 1% nitric acid blank was also prepared. For particle transport studies, a 50 ng mL^{-1} stock solution of dissolved elemental standards were prepared in ultrapure water. Aliquots of the stock solution were spiked with a reference AuNP suspension to create five different samples with particle number concentrations ranging from 2.6×10^4 to 1.8×10^5 particles mL^{-1}; these number concentrations were selected to enable detection of ~ 20 particles s^{-1} for 100% transport efficiency at the various sample flow rates tested. Each sample made was used for two liquid flow rates. It was necessary to prepare solutions with varying concentrations as a function of

This journal is © The Royal Society of Chemistry 2023

J. Anal. At. Spectrom., 2023, **38**, 721–729 | **723**

Fig. 2 Rendering of sample introduction system. (A) Sample introduction chamber with the lid of the device–housing chamber removed to show position of cVVSI nebulizer. (B) Sectional view of the chamber showing the design of the curtain gas introduction; the current gas flows through the 3D-printed tubes to the patterned gas inlets and into the aerosol transport chamber (into the plane of the paper). The red dashed line in (A) indicates the slicing plane for (B). Blue arrows are to emphasize the locations of gas introduction.

flow rate to ensure that each particle event detected corresponds to one nanoparticle, *i.e.* to eliminate coincident particle events.[36]

Data analysis

Particle data was processed using time-of-flight single particle investigator (TOF SPI), which is an in-house developed LabVIEW program (LabVIEW 2018, National Instruments Corp., Austin, TX, USA) for spICP-TOFMS data analysis. TOF SPI was used to find and count AuNP events. Net signals and concentration detection limits were calculated as two-tailed detection limits with false-positive (α) and false-negative (β) rates of 5% as described by Currie and recommended by the IUPAC.[37,38] However, since ICP-TOFMS signals following a compound-

Poisson distribution,[39] an in-house LabVIEW program ("Lc-Ld Expression-Calc") was used to estimate detection limits. Determination of detection limits with noised modeled as normal or Poisson–normal underestimates the true detection limit. The LabVIEW program used to estimate ICP-TOFMS detection limits is available on our group's github page: **https://github.com/TOFMS-GG-Group**.

Results and discussion

Transport efficiency study

We measured the transport efficiency and absolute sensitivities for a range of elements (Co, Y, In, Cs, Ce, and U) at liquid flow rates from 5–50 μL min^{-1} for the cVSSI-based sample
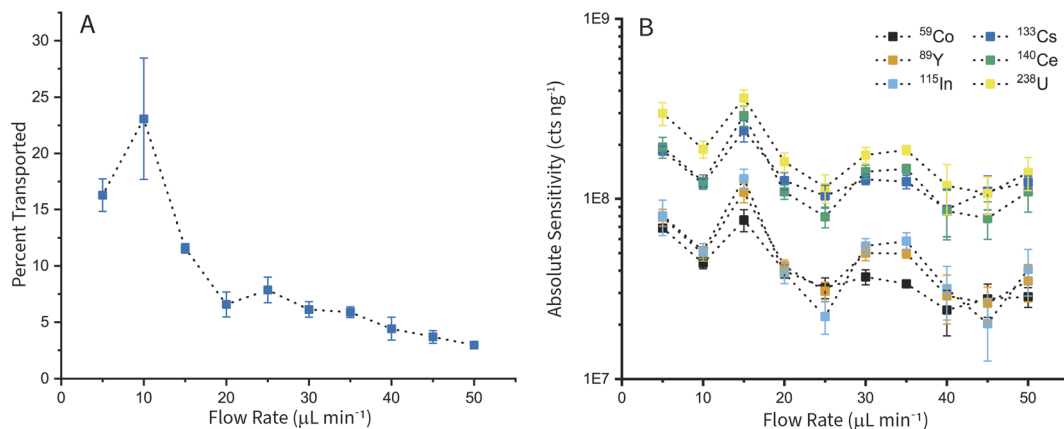
724 | *J. Anal. At. Spectrom.*, 2023, **38**, 721–729

This journal is © The Royal Society of Chemistry 2023

Fig. 3 (A) Plot showing the transport efficiency across a series of flow rates, from 5–50 μL min^{-1}; transport efficiencies were calculated using the particle method. (B) Plot of absolute sensitivities for dissolved elements across the same flow rates.

introduction system. In these experiments, we kept transport gas flow rates, cVSSI peak-to-peak voltage (V_{piezo}) and frequency (f_{piezo}) to drive the piezoelectric transducer, and ICP-TOFMS conditions constant. Samples used for measurements contained dissolved elemental standards and known number concentrations of 50 nm AuNPs. Measurements of 60 s in duration were collected in triplicate, excluding the 50 μL min^{-1} flow rate measurement, which was made in duplicate. The average value across replicates is reported with error bars as the standard deviation. To calculate transport efficiency (η_{neb}), the number of particles detected per unit time ($N_{NP,detected}$) is divided by the predicted flux of particles through the nebulizer ($N_{NP,neb}$) as shown in eqn (1). This method for determining transport efficiency is known as the "particle number method" and was developed for single-particle ICP-MS measurements.[40]

$$\eta_{neb} = \frac{N_{NP,detected}}{N_{NP,neb}} \quad (1)$$

Fig. 3 shows the transport efficiencies of particles and absolute sensitivities for dissolved elements at each flow rate. To calculate absolute sensitivities, first the transport efficiency found for the respective flow rate (q_{neb}) is used to calculate the plasma uptake rate (q_{plasma}) in mL s^{-1} (eqn (2)). Then, the relative sensitivity for each element i ($S_{neb,i}$) in cts s^{-1} ng^{-1} mL^{-1} is divided by q_{plasma} to result in the absolute sensitivity of each element i ($S_{p,i}$) in cts ng^{-1} (eqn (3)).

$$\eta_{neb} \times q_{neb} = q_{plasma} \quad (2)$$

$$\frac{S_{neb,i}}{q_{plasma}} = S_{p,i} \quad (3)$$

Fig. 3 shows that the flow rate for the highest particle transport (Fig. 3A) and the highest absolute sensitivity for dissolved elements (Fig. 3B) are not correlated. The highest transport efficiency of particles is observed at 23% with a standard deviation of 5.4% at a sample flow rate of 10 μL min^{-1}. The highest absolute sensitivity for dissolved elements is observed

at 15 μL min^{-1} with 2.91 × 10^8 counts ng^{-1} of Ce and a standard deviation of 3.37 × 10^7 counts ng^{-1}. The higher standard deviation for transport efficiency at 10 μL min^{-1} is due to a combination of insufficient time given for sample uptake and irregular nebulization behavior at this low flow rate. With flow rates of 10 μL min^{-1} or lower, we have sometimes observed (on the benchtop) pulsating, on-and-off, nebulization behavior from the cVSSI device. For best performance, f_{piezo}, V_{piezo}, and gas flows should be optimized for each liquid flow rate. We did not do such a multi-parameter optimization for the data in Fig. 3 in order to isolate the effect of liquid flow rate on transport efficiency.

As previously observed with pneumatic nebulization, in our nebulization device, higher transport efficiencies and sensitivities are obtained at lower liquid flow rates.[41] This is likely due to the smaller size of droplets in the aerosol. Smaller droplets are transported more efficiently by gas flows and are more completely vaporized in the plasma. With the cVSSI nebulizer, at 10 and 15 μL min^{-1}, the average droplet sizes are 11.6 and 14.7 μm, respectively. At 50 μL min^{-1}, the average droplet size increases to 24.3 μm. We report our droplet sizing procedure in the ESI,† and results of the droplet sizing in Fig. S3 and S4.† Based on the results of this study, 15 μL min^{-1} was chosen as the optimal flow rate for subsequent experiments.

Voltage and frequency input study

One of the unique features of cVSSI as a nebulization device is the ability to tune the aerosol generation using the frequency and voltage applied to the piezoelectric transducer. To optimize the frequency and voltage of the cVSSI nebulizer device, we recorded ICP-TOFMS measurements with a series of peak-to-peak voltages (V_{piezo}) and frequencies (f_{piezo}) to drive the piezoelectric transducer, while keeping all other variables (i.e. solution composition, gas flows, liquid flow, instrument parameters) constant. In Fig. 4A–E, the sensitivities measured for Co, Y, In, Ce, and U from a 10 ng mL^{-1} multi-element solution are plotted at the different V_{piezo} and f_{piezo} values. At all V_{piezo} values, we found similarly shaped response curves for

This journal is © The Royal Society of Chemistry 2023

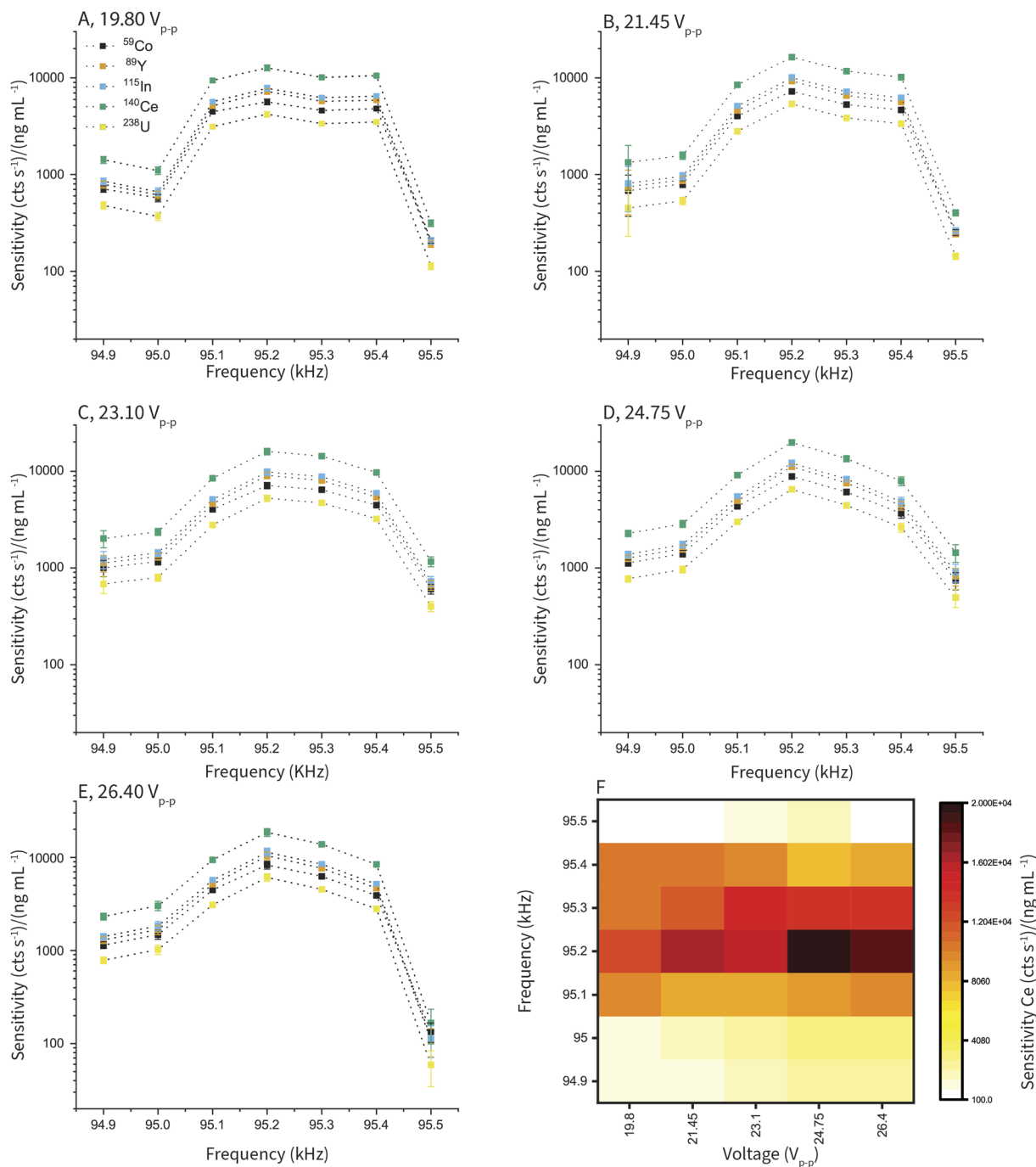J. Anal. At. Spectrom., 2023, **38**, 721–729 | **725**

Fig. 4 (A)–(E) Plots of sensitivity for several elements (Co, Y, In, Ce, and U) across the selected voltage and frequency range. Voltage input for each plot is shown. Error bars give the standard deviation of the measurement. (F) Heat map showing the sensitivities measured for ^{140}Ce across the entire input range.

all elements as a function of f_{piezo} and we also found the same optimal f_{piezo} independent of the V_{piezo} applied. Overall, the sensitivity is more affected by f_{piezo} than V_{piezo}. However, as seen in Fig. 4F, the best absolute response depends on both frequency and voltage. For the device tested, highest sensitivity is seen at $f_{piezo} = 95.2$ kHz and $V_{piezo} = 24.75$ V; at these optimum conditions, we recorded a sensitivity of 1.98×10^4 cts s^{-1} ng^{-1} mL^{-1} of ^{140}Ce with a RSD of 6.5%. The stability of the signal can also be affected by the voltage and frequency applied

to the piezoelectric transducer. Signal stability seems to be controlled primarily by V_{piezo}; this is illustrated in Fig. S5,† which shows ICP-TOFMS time traces for ^{140}Ce$^+$ with $V_{piezo} = 14.19$ and 23.76 V and $f_{piezo} = 96.96$ kHz. When V_{piezo} increased from 14.19 to 23.76 V, the RSD of the steady-state measurement decreased from 20% to 4.0%.

The optimal cVSSI frequencies and voltages vary from device to device. Each device's operational V_{piezo} and f_{piezo} ranges are found on the benchtop before fitting the device into the sample

726 | J. Anal. At. Spectrom., 2023, 38, 721–729

This journal is © The Royal Society of Chemistry 2023

Table 1 Analytical figures of merit for the cVSSI sample introduction system

Element	Linearity, slope	Sensitivity (cts s^{-1} ng^{-1} mL^{-1})	L_D (cps)	$X_D^{Conc.}$ (ng mL^{-1})	BEC (ng mL^{-1})
^{59}Co	1.058 ± 0.02	8100 ± 1300	91	0.011	0.075
^{89}Y	1.045 ± 0.02	$13\,000 \pm 1700$	61	0.005	0.020
^{115}In	1.11 ± 0.04	$20\,000 \pm 4900$	220	0.011	0.179
^{140}Ce	1.081 ± 0.03	$21\,000 \pm 4100$	160	0.008	0.098
^{166}Er	1.044 ± 0.02	4100 ± 510	17	0.004	0.004
^{209}Bi	1.064 ± 0.03	$10\,000 \pm 1700$	48	0.005	0.017
^{238}U	1.066 ± 0.02	6700 ± 1100	64	0.009	0.043

introduction chamber. Further optimization of V_{piezo} and f_{piezo} is completed as part of daily tuning procedures to optimize ICP-MS signal levels. As illustrated in Fig. 4, tuning can be accomplished rapidly by first optimizing f_{piezo}, which is independent of V_{piezo}, and then optimizing V_{piezo}. Operational parameters for the cVSSI device for all experiments are provided in Table S1.†

Calibrations and detection limits

To obtain net signal detection limits (L_D), concentration detection limits ($X_D^{Conc.}$), and elemental sensitivities, background-subtracted calibration curves were generated from collected ICP-TOFMS signals (Fig. S6†). Using the average blank

single (λ) in counts s^{-1} for each element of interest, eqn (4) is used to calculate L_D values. The L_D expression is estimated using false positive (α) and false negative (β) rates of 5% (ref. 37) and a Monte Carlo simulation that combines noise due to Poisson statistics and the detector response function of the TOFMS detector.[39]

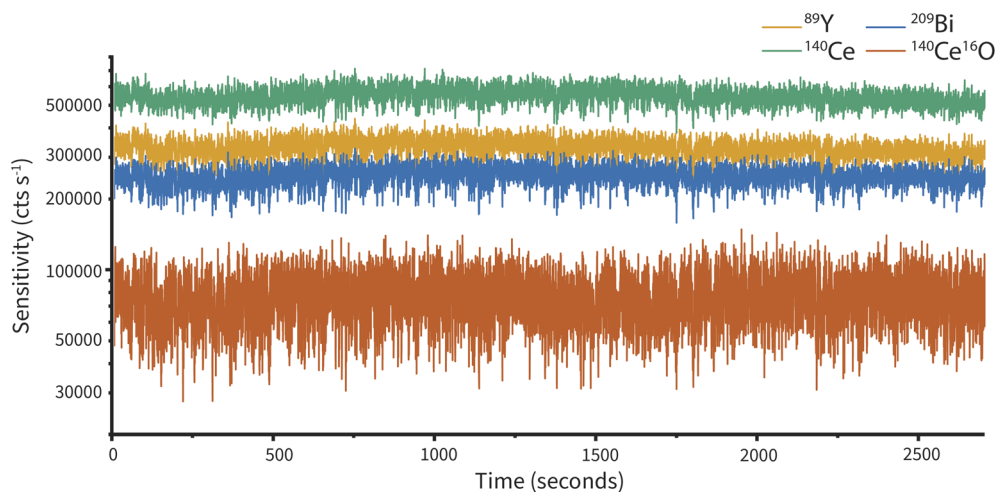$$L_D = 3.65 \times \lambda^{0.5} + 3.14 \tag{4}$$

The calibration curves display good linearity with best-fit slopes of the log–log plots all near 1.0. Background equivalent concentrations (BEC) are all below 0.200 ng mL^{-1}. L_D values are all below 250 cts s^{-1} and correspond to $X_D^{Conc.}$ values of 0.011 ng mL^{-1} and lower; values for each element analyzed are reported in Table 1.

Long term stability

To evaluate the stability of the cVSSI nebulization device, we recorded ICP-TOFMS signal with continuous sample introduction (15 μL min^{-1}) into the cVSSI nebulizer for 45 minutes. A 10 ng mL^{-1} multi-element solution was used for this measurement. Fig. 5 shows the time trace for three of the seven elements measured. Table 2 gives RSD values and predicted RSD values based on Poisson statistics for all elements measured. All measured RSD values are found to be below 10%, but are substantially higher than count-limited Poisson RSD values.

Table 2 Measured RSD and predicted Poisson RSD values for long term stability measurement

Element	RSD (%)	Poisson-predicted RSD (%)
^{59}Co	8.8	0.42
^{89}Y	8.6	0.32
^{115}In	9.1	0.25
^{140}Ce	8.0	0.25
^{166}Er	8.8	0.55
^{209}Bi	9.0	0.37
^{238}U	8.4	0.43

Fig. 5 Time trace showing the stability of several signals over a period of 45 minutes.

This journal is © The Royal Society of Chemistry 2023

J. Anal. At. Spectrom., 2023, **38**, 721–729 | **727**

The elevated RSD is well established for ICP-MS and is due mostly to flicker noise from the plasma, though some additional noise from the cVSSI nebulization source could contribute. As seen in Fig. 5, we observe minimal long-term drift (across 45 min), making cVSSI nebulization a viable candidate for techniques requiring long analysis times, such as in combination with separation approaches.

To characterize noise affecting more than one mass channel, error in the $^{167}Er : ^{168}Er$ ratio is reported. The measured RSD of the $^{167}Er : ^{168}Er$ signal ratio is 1.6%, while the predicted RSD from Poisson statistics is 0.93%. The agreement of $^{167}Er : ^{168}Er$ ratio precision with Poisson statistics indicates that additional noise components for single-nuclide measurements are mostly from correlated noise sources, such as $1/f$ noise.

To further characterize the noise in the measurements, a 1000-point fast Fourier transformation of the ICP-TOFMS data is performed using Origin 2019b (OriginLab, Northampton, MA, USA). Noise amplitude is converted to decibels (dB) as previously described.[42] The noise power spectra are plotted in Fig. S7.† In the noise power spectra, no obvious peaks are present, indicating noise at specific frequencies. White noise measured for all elements averaged at 55 dB or below, and $1/f$ noise is also observed, although appears to be a small contributor to the overall noise as expected with low long-term drift.

Conclusion

When integrated with ICP-MS, cVSSI functions as a continuous nebulization device that performs best when combined with low liquid flow rates (<15 µL min^{-1}). In the cVSSI device, nebulization processes are independent of gas flows, which allows for more flexibility while tuning for nebulization efficiency and transport gases. Additionally, each cVSSI nebulizer is a fraction of the cost of traditional pneumatic nebulizers; the cost of consumable components is about $3 USD per device.

The results presented in this work are encouraging for the future of cVSSI as a nebulization device for ICP-MS analysis. In order to match the performance of conventional sample introduction systems, this system requires additional optimization to reduce device to device variability as well as to increase the stability of nebulization and the transport efficiency of the system. In future work, low cost of each device gives the possibility of routinely replacing nebulizers when working with samples having high solid concentrations that may cause clogging or contamination. Many techniques currently using pneumatic nebulization that require low sample flow rates could be adapted to the cVSSI sample introduction system, including separation techniques that require nebulization to occur at the low flow rates at which the separation is carried out. With further optimization, a high efficiency cVSSI sample introduction system could be created.

Conflicts of interest

There are no conflicts to declare.

Acknowledgements

References

1 R. F. Browner and A. W. Boorn, *Anal. Chem.*, 1984, **56**, 786A–798A.

2 J.-L. Todoli and J.-M. Mermet, in *Liquid Sample Introduction in ICP Spectrometry*, ed. J.-L. Todoli and J.-M. Mermet, Elsevier, Amsterdam, 2008, ch. 2, pp. 3–15.

3 R. N. Kniseley, H. Amonson, C. C. Butler and V. A. Fassel, *Appl. Spectrosc.*, 1974, **28**, 285–286.

4 J. A. Burgener, *US Pat.*, 5411208, 1995.

5 F. Vanhaecke, M. van Holderbeke, L. Moens and R. Dams, *J. Anal. At. Spectrom.*, 1996, **11**, 543–548.

6 H. S. Tan, *US Pat.*, 5884846, 1999.

7 K. Inagaki, S.-i. Fujii, A. Takatsu and K. Chiba, *J. Anal. At. Spectrom.*, 2011, **26**, 623–630.

8 M. Grotti, A. Terol and J. L. Todolí, *TrAC, Trends Anal. Chem.*, 2014, **61**, 92–106.

9 J. L. Todolí and J. M. Mermet, *Spectrochim. Acta, Part B*, 2006, **61**, 239–283.

10 T. Robert, *Practical Guide to ICP-MS: A Tutorial*, CRC Press, Boca Raton, FL, 3rd edn, 2013.

11 J. W. Olesik, J. A. Kinzer and B. Harkleroad, *Anal. Chem.*, 1994, **66**, 2022–2030.

12 H. Liu, R. H. Clifford, S. P. Dolan and A. Montaser, *Spectrochim. Acta, Part B*, 1996, **51**, 27–40.

13 K. E. Lawrence, G. W. Rice and V. A. Fassel, *Anal. Chem.*, 1984, **56**, 289–292.

14 J. A. McLean, H. Zhang and A. Montaser, *Anal. Chem.*, 1998, **70**, 1012–1020.

15 A. Montaser, J. A. McLean and J. M. Kacsir, *US Pat.*, 6166379, 2000.

16 J.-L. Todolí and J.-M. Mermet, *J. Anal. At. Spectrom.*, 2002, **17**, 345–351.

17 F. Ardini, M. Grotti, R. Sánchez and J. L. Todolí, *J. Anal. At. Spectrom.*, 2012, **27**, 1400–1404.

18 S. Martínez, R. Sánchez and J.-L. Todolí, *J. Anal. At. Spectrom.*, 2022, **37**, 1032–1043.

19 J. A. Burgener and Y. Makonnen, in *Sample Introduction Systems in ICPMS and ICPOES*, ed. D. Beauchemin, Elsevier, Amsterdam, 2020, ch. 2, pp. 57–142.

20 J.-L. Todolí and J.-M. Mermet, *J. Anal. At. Spectrom.*, 2001, **16**, 514–520.

21 M. A. Tarr, G. Zhu and R. F. Browner, *Anal. Chem.*, 1993, **65**, 1689–1695.

22 G. M. Hieftje and H. V. Malmstadt, *Anal. Chem.*, 1968, **40**, 1860–1867.

23 J. O. Orlandini v. Niessen, J. N. Schaper, J. H. Petersen and N. H. Bings, *J. Anal. At. Spectrom.*, 2011, **26**, 1781–1789.

728 | *J. Anal. At. Spectrom.*, 2023, **38**, 721–729

This journal is © The Royal Society of Chemistry 2023

24 J. W. Olesik and S. E. Hobbs, *Anal. Chem.*, 1994, **66**, 3371–3378.

25 K. Shigeta, H. Traub, U. Panne, A. Okino, L. Rottmann and N. Jakubowski, *J. Anal. At. Spectrom.*, 2013, **28**, 646–656.

26 T. Vonderach and D. Günther, *J. Anal. At. Spectrom.*, 2021, **36**, 2617–2630.

27 N. Ranganathan, C. Li, T. Suder, A. K. Karanji, X. Li, Z. He, S. J. Valentine and P. Li, *J. Am. Soc. Mass Spectrom.*, 2019, **30**, 824–831.

28 S. N. Majuta, C. Li, K. Jayasundara, A. Kiani Karanji, K. Attanayake, N. Ranganathan, P. Li and S. J. Valentine, *J. Am. Soc. Mass Spectrom.*, 2019, **30**, 1102–1114.

29 A. DeBastiani, S. N. Majuta, D. Sharif, K. Attanayake, C. Li, P. Li and S. J. Valentine, *ACS Omega*, 2021, **6**, 18370–18382.

30 S. N. Majuta, A. DeBastiani, P. Li and S. J. Valentine, *J. Am. Soc. Mass Spectrom.*, 2021, **32**, 473–485.

31 J. Wang, C. Li and P. Li, *J. Am. Soc. Mass Spectrom.*, 2022, **33**, 304–314.

32 D. Sharif, S. H. Foroushani, K. Attanayake, V. K. Dewasurendra, A. DeBastiani, A. DeVor, M. B. Johnson, P. Li and S. J. Valentine, *J. Phys. Chem. B*, 2022, **126**, 8970–8984.

33 D. F. Thompson, *J. Anal. At. Spectrom.*, 2014, **29**, 2262–2266.

34 V. Geertsen, E. Barruet and O. Taché, *J. Anal. At. Spectrom.*, 2015, **30**, 1369–1376.

35 X. Li, K. Attanayake, S. J. Valentine and P. Li, *Rapid Commun. Mass Spectrom.*, 2018, **35**, e8232.

36 F. Laborda, J. Jiménez-Lamana, E. Bolea and J. R. Castillo, *J. Anal. At. Spectrom.*, 2011, **26**, 1362–1371.

37 L. A. Currie, *Pure Appl. Chem.*, 1995, **67**, 1699–1723.

38 L. A. Currie, *Anal. Chim. Acta*, 1999, **391**, 127–134.

39 A. Gundlach-Graham, L. Hendriks, K. Mehrabi and D. Günther, *Anal. Chem.*, 2018, **90**, 11847–11855.

40 M. D. Montaño, J. W. Olesik, A. G. Barber, K. Challis and J. F. Ranville, *Anal. Bioanal. Chem.*, 2016, **408**, 5053–5074.

41 J. W. Olesik, J. A. Hartshorne, N. Casey, E. Linard and J. R. Dettman, *Spectrochim. Acta, Part B*, 2021, **176**, 106038.

42 F. Monna, J.-L. Loizeau, B. Thomas, C. Guéguen, P.-Y. Favarger, R. Losno and J. Dominik, *Analusis*, 2000, **28**, 750–757.

This journal is © The Royal Society of Chemistry 2023

J. Anal. At. Spectrom., 2023, **38**, 721–729 | 729